

Sea Wind Retrieval by Analytically-Based Geophysical Model Functions and Sentinel-1A SAR Images

Nafiseh Radkani and Bijan Zakeri*

Abstract—In this paper, the sea surface wind speeds are retrieved by using an analytical scattering model, so called the analytically-based geophysical model function (GMF), from C-band Sentinel-1A VV-polarized synthetic aperture radar (SAR) images. The analytical models accurately simulate the rough surface scattering in the incidence angles range of SARs. The accuracy of the scattering results of the models depends on the sea wave spectrum. In this work, the effect of the sea spectral models on the accuracy of the sea surface wind speed retrieving is evaluated. In this regard, for omnidirectional and directional parts of sea spectrum, the Elfouhaily/Hwang spectra and Elfouhaily/McDaniel’s models are employed, respectively. The VV-polarized backscattered normalized radar cross-section (NRCS) is calculated by using the first-order small-slope approximation (SSA1) with the four composite models of the mentioned omnidirectional spectra and angular spreading functions (directional part), and the backscattering results are compared with the empirical model CMOD6. Then, from the VV-polarized Sentinel-1A SAR data in two resolutions, the wind speeds are estimated by the analytical and empirical models. The comparison of analytical models with CMOD6 shows that Hwang-Elfouhaily model is the best among the composite models. The results show that the analytical scattering models can be easily used for the sea wind speed retrieving below 20 m/s.

1. INTRODUCTION

Synthetic aperture radars (SARs) measure the high-resolution backscattered normalized radar cross-section (NRCS) of sea surface roughness. Sea surface roughness and its NRCS accordingly are strongly influenced by the local winds. Consequently, SAR measurements are the resources for local wind field retrieval above the sea surfaces. The accuracy of the wind field retrieval from SARs depends on the modelling of backscattered signals from sea surface roughness.

For wind field estimation from scatterometer or SAR data, geophysical model functions (GMFs) are commonly used. GMFs relate the NRCS of wind cells to local winds, satellite observation geometry, and other marine physical parameters. The common GMFs in C-band are CMOD functions, e.g., CMOD5 [1], CMOD5.N [2], and CMOD6 [3] which are usually constructed empirically based on the measurements of satellite scatterometers, weather prediction models, and buoys data. Though the resolution of scatterometers is low (in kilometer scales), CMOD functions can be used for wind speed retrieval from high-resolution (in meter scales) SAR data [4, 5]. Recently, GMFs, i.e., C-SARMOD [6] and C-SARMOD2 [7] functions, have been constructed empirically based on high-resolution measurements of C-band SARs for coastal wind retrieval.

Empirical GMFs do not have the capability to describe and interpret sea phenomena. Therefore, the development of electromagnetic scattering models to calculate the scattering is an important issue. The electromagnetic scattering models for simulating the rough surface scattering have been divided into exact numerical and approximate analytical methods. The exact numerical methods, e.g.,

Received 27 March 2019, Accepted 12 June 2019, Scheduled 26 June 2019

* Corresponding author: Bijan Zakeri (zakeri@nit.ac.ir).

The authors are with the Faculty of Electrical and Computer Engineering, Babol Noshirvani University of Technology, Babol, Iran.

method of moments (MoM) [8] and finite-difference time-domain (FDTD) [9], can be applied to the problem of rough surface scattering. However, these methods are not efficient for electrically large surfaces (high wind speeds). The approximate analytical methods are small perturbation method (SPM) [10, 11], Kirchhoff approximation (KA) [10, 11], AIEM [12], two-scale model (TSM) [13], and small-slope approximation (SSA) [14–20]. SPM and KA calculate the scattering of small and large-scale roughness, respectively, while TSM, AIEM and SSA, so-called unified models, describe the scattering of both types. The earlier versions of TSM combine the SPM and KA, and they are sensitive to a cutoff parameter for separation of sea wave scales, while recent TSMs [13] employ the SSA method instead of SPM that has no need of a cutoff parameter. The SSA method bridges between the SPM and KA without separation of sea wave scales. The SSA method has been developed in two orders of accuracy; first-order (SSA1) and second-order (SSA2). For the scattering from sea surfaces at C-band frequency, the difference between the two versions is relatively small, while the computations of the SSA1 are much faster than the SSA2.

In order to calculate the scattering from sea surfaces using analytical methods, either the sea spectrum or autocorrelation function of surface height is required. Sea spectrum has a directional shape, which includes an omnidirectional part and an angular spreading function (directional part). Various functions have been proposed in the literature based on *in-situ* and laboratory measurements for both parts such as the directional spectra proposed by Apel [21], Romeiser et al. [22], Elfouhaily et al. [23], the omnidirectional spectrum proposed by Hwang et al. [24–27], and the angular spreading function proposed by McDaniel [14]. Elfouhaily spectrum is the most common sea spectrum used for simulating the sea surface scattering in the literature [16–19]. Hwang spectrum is the newest spectrum for sea waves that includes swell effects on sea roughness. The accuracy of scattering models of sea surfaces depends on the accuracy of sea spectrum. Small-scale waves or Bragg waves have a dominant contribution to sea surface scattering in the microwave regime. Therefore, the sea spectrum should include a wide range of wave scales and accurately represent small-scale waves.

In this paper, sea wind speeds are retrieved from Sentinel-1A SAR images by using an analytical method, so-called the analytically-based GMF, which employs the SSA1 with various composite spectra. First, we compare the omnidirectional part of Elfouhaily spectrum with Hwang spectrum and Elfouhaily angular function with McDaniel function, especially in Bragg wavenumber range. Then, the backscattering from sea surface for four compositions of the mentioned omnidirectional spectra and angular spreading functions, Elfouhaily-El fouhaily (E-E), Hwang-El fouhaily (H-E), Elfouhaily-McDaniel (E-M), and Hwang-McDaniel (H-M), is simulated by the SSA1 model and compared with empirical CMOD6 function as a reference model. Next, by using wind directions, given by a weather prediction model, the sea wind speeds are estimated from VV-polarized SAR images in two different resolutions using the SSA1 model with various spectra. The results have been compared with CMOD6's estimated wind speeds. In these regards, the most appropriate spectra with respect to various situations, leading to accurate retrievals, are reported.

This paper is organized as follows. In Section 2, the sea wave spectral model and formulation of SSA1 method are described. The comparison of various sea spectra and the comparison of the analytical scattering model with empirical CMOD6 function are given in Section 3. Wind speed estimation using the SSA1 model and empirical model is described in Section 4. Section 5 concludes the paper.

2. MODELING OF SEA SCATTERING

2.1. Sea Spectrum

The sea surface waves are considered as a stationary random process, and they are described statistically by a spectral model. The sea spectrum can be obtained by the inverse Fourier transform of the autocorrelation of sea height, and it has a directional form which can be expressed as

$$W(k, \varphi_k) = W_0(k) \cdot f(k, \varphi_k) \quad (1)$$

where $W_0(k)$ is the omnidirectional part of the spectrum, and $f(k, \varphi_k)$ is its angular spreading function. k is the wave wavenumber, and φ_k is the wave direction relative to the wind direction. The omnidirectional part is the function of sea wind speed, while the angular spreading function is

the function of both wind speed and wind direction. The best description for the form of the angular spreading function is proposed by Elfouhaily et al. [23] in the following form

$$f(k, \varphi_k) = [1 + \Delta k \cos(2\varphi_k)] / 2\pi \tag{2}$$

This relation can be adjusted to all other proposed spreading functions using the following ratio

$$\Delta k = \frac{f(k, 0) - f(k, \pi/2)}{f(k, 0) + f(k, \pi/2)} \tag{3}$$

where 0° and $\pi/2$ correspond to upwind and crosswind directions, respectively. The sea wave spectrum should include a wide range of sea waves from short capillary to long gravity waves.

2.2. Backscattering NRCS

In C-band, the backscattering NRCS of the sea surface for co-polarizations (VV or HH) can be expressed as

$$\sigma^{pq}(\theta, \varphi; u_{10}) = \sigma_0^{pq}(\theta; u_{10}) + \sigma_1^{pq}(\theta; u_{10}) \cos \varphi + \sigma_2^{pq}(\theta; u_{10}) \cos(2\varphi) \tag{4}$$

where p and q denote the polarizations of scattered and incident waves, respectively. φ is the angle between radar range direction and wind direction (wind relative direction), θ the incident (or observation) angle, and u_{10} the wind speed at 10 meters above sea level. σ_0 includes the wind speed scale information. σ_1 is related to upwind/downwind asymmetry and resolves 180° ambiguity in wind direction. σ_2 is related to upwind/crosswind asymmetry and determines the wind direction. For sea surfaces with Gaussian statistics, $\sigma_1 = 0$.

2.3. Small-Slope Approximation

The small-slope approximation (SSA) is an analytical model used to simulate the scattering from a random rough surface, and in this work, the first-order SSA (SSA1) is used. For the Gaussian sea surfaces, the backscattering coefficients of Eq. (4) in the SSA1 can be expressed as [17]

$$\sigma_0^{pq}(\theta; u_{10}) = \frac{2|B_1^{pq}(\theta)|^2}{Q_z^2} e^{-Q_z^2 \sigma_h^2} \int_0^\infty J_0(k_B r) \left[e^{Q_z^2 C_0(r)} I_0(Q_z^2 C_2(r) - 1) \right] r dr \tag{5}$$

$$\sigma_2^{pq}(\theta; u_{10}) = \frac{4|B_1^{pq}(\theta)|^2}{Q_z^2} e^{-Q_z^2 \sigma_h^2} \int_0^\infty e^{Q_z^2 C_0(r)} J_2(k_B r) I_1(Q_z^2 C_2(r)) r dr \tag{6}$$

where $Q_z = q_0 + q_k$, and $-q_0$ and q_k are the vertical projections of the incident and scattered wave vectors, respectively. B_1 is the first-order Bragg kernel and depends on the scattering geometry and dielectric constant of the medium [17]. J_m denotes the Bessel function of the first kind and of order n , and I_m denotes the modified Bessel function of the first kind and of order m . $k_B = 2K_0 \sin \theta$ is the Bragg wavenumber (K_0 is free space wavenumber). $C_0(r)$ is the isotropic part of the height correlation function, and $C_2(r)$ is its anisotropic part. They are computed from the omnidirectional part of sea spectrum $W_0(k)$ and its spreading function by following expressions

$$C_0(r) = \int_0^\infty W_0(\xi) J_0(r\xi) d\xi \tag{7}$$

$$C_2(r) = \int_0^\infty W_0(\xi) \Delta(\xi) J_2(r\xi) d\xi \tag{8}$$

The integrations are performed over $\xi \in [\xi_{\min}, \xi_{\max}]$ with $\xi_{\min} = 0.25k_p$ (k_p called peak wavenumber [23]) and $\xi_{\max} = 4K_0$. $\sigma_h^2 = C_0(0)$ is the height variance. The integrations over r and ξ are done in logarithmic scales.

3. SCATTERING SIMULATIONS

3.1. Comparison of Sea Spectra

In order to calculate the scattering from the sea surface, we use various sea spectra. The spectra proposed by Elfouhaily et al. [23] and by Hwang et al. [24–27] are considered as omnidirectional part of the spectrum, and the angular spreading functions proposed by Elfouhaily et al. [23] and McDaniel [14] are considered as directional part of the spectrum.

The Elfouhaily omnidirectional spectrum and Hwang spectrum are plotted in Fig. 1 for the wind speeds of 5, 10, 15, and 20 m/s for a fully-developed sea. The behaviours of the two spectra are similar. Also, the wind speed effects on the spectra are similar. The Bragg waves have a dominant contribution to the sea surface scattering. Therefore, the part of the wave spectrum corresponding to the small-scale waves (high wavenumbers) should be attended. Sentinel-1A is a high-resolution C-band SAR instrument and operates at 5.405 GHz and dual polarizations (VV and HV). The SAR images can be acquired by interferometric wide swath (IWS) mode, in which for this mode, incident angle range is approximately 30° – 45° . According to this range, Bragg wavenumber range is between $k_{B1} = 113.2$ rad/m and $k_{B2} = 160$ rad/m, where these values are shown in the figure by the dashed black line, and the curves belonging to this range are replotted larger. In this range, the curves are close together. Also, the energy of Hwang spectrum is more than Elfouhaily spectrum, especially at

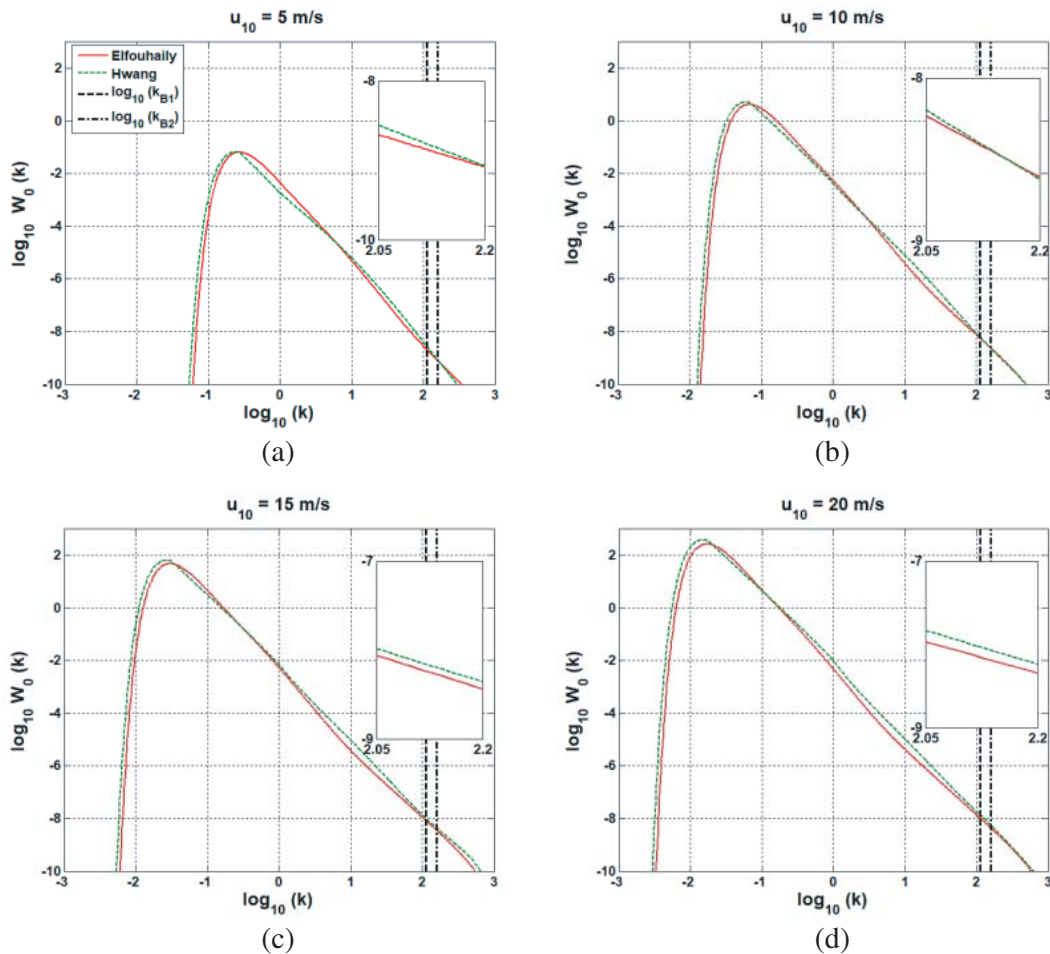


Figure 1. Elfouhaily omnidirectional spectrum and Hwang spectrum at $u_{10} =$ (a) 5 m/s, (b) 10 m/s, (c) 15 m/s and (d) 20 m/s. Bragg wavenumbers in the C-band with incident angles 30° and 45° are denoted.

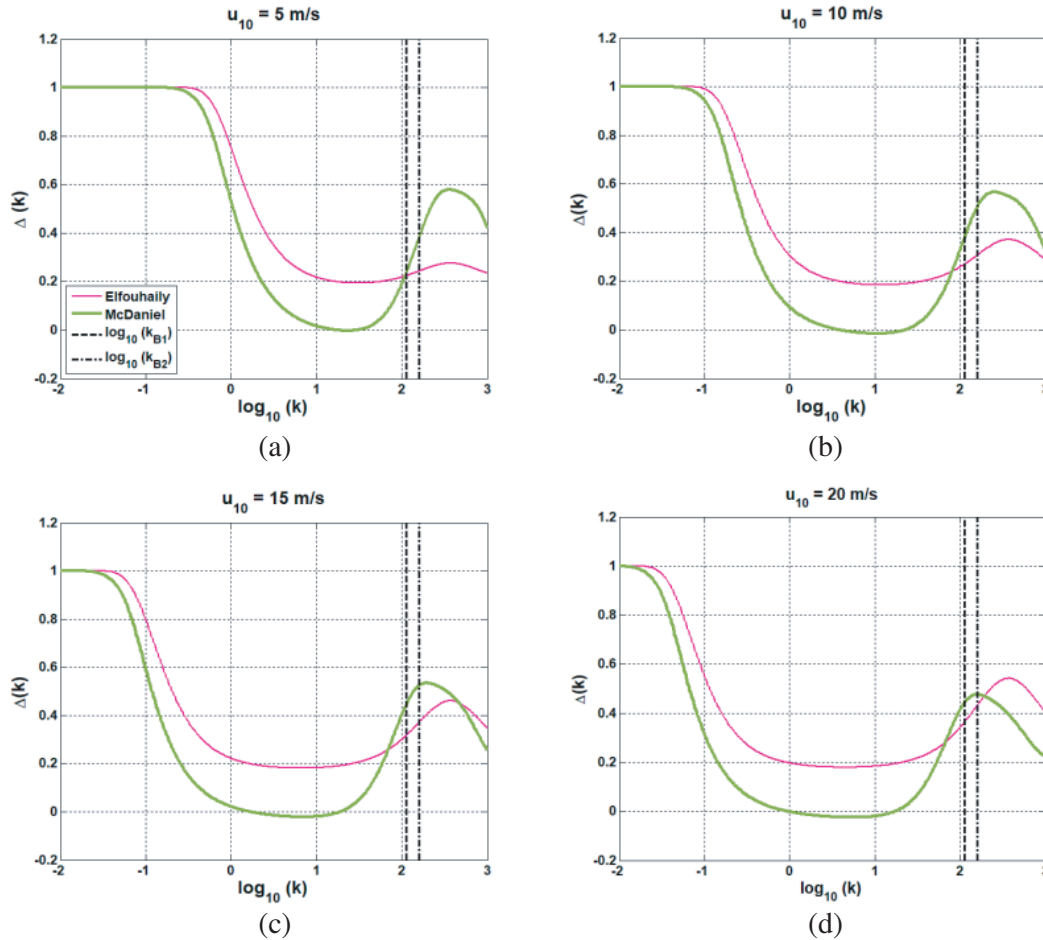


Figure 2. $\Delta(k)$ ratios related to the spreading functions proposed by Elfouhaily and by McDaniel in terms of logarithm of wavenumber at $u_{10} =$ (a) 5 m/s, (b) 10 m/s, (c) 15 m/s and (d) 20 m/s. Bragg wavenumbers in the C-band with incident angles 30° and 45° are denoted.

high wind speeds (Figs. 1(c) and (d)).

In Fig. 2, $\Delta(k)$ ratios related to the Elfouhaily and McDaniel spreading functions are seen at various wind speeds. The two curves have similar behaviours in the range of large-scale waves (low wavenumbers). At high wavenumbers and in Bragg waves region, the McDaniel function yields greater directionality than the Elfouhaily function.

3.2. Comparison of Scattering Coefficients

Scattering simulations are performed at the frequency of 5.405 GHz (C-band) with the relative dielectric constant of $\epsilon_r = 67 + 35i$ [28]. The backscattering from sea surfaces is simulated by the SSA1 model with different compositions of omnidirectional spectra and spreading functions; E-E, E-M, H-E, and H-M and the results are compared with the curves of CMOD6 function. The CMOD6 is an empirical correction of the CMOD5.N GMF, and its formulation is found in [2, 3]. The VV-polarized backscattering NRCSs in terms of wind speed are plotted in Fig. 3 for wind directions of 0° , 45° , 90° , and 180° , whereas the scattering results depend on the incident angle. The results are plotted for incident angles of 30° and 45° according to the incident angle range of Sentinel-1A SAR images in IWS mode. The wind speed range is 2–30 m/s.

As seen in Fig. 3, the accuracies of scattering results depend on wind speed, wind direction, and incident angle. It can be seen that backscattering NRCSs increase with wind speed, except for the spectra with Elfouhaily spreading function at high wind speeds (Fig. 3(g)). According to Figs. 3(c)

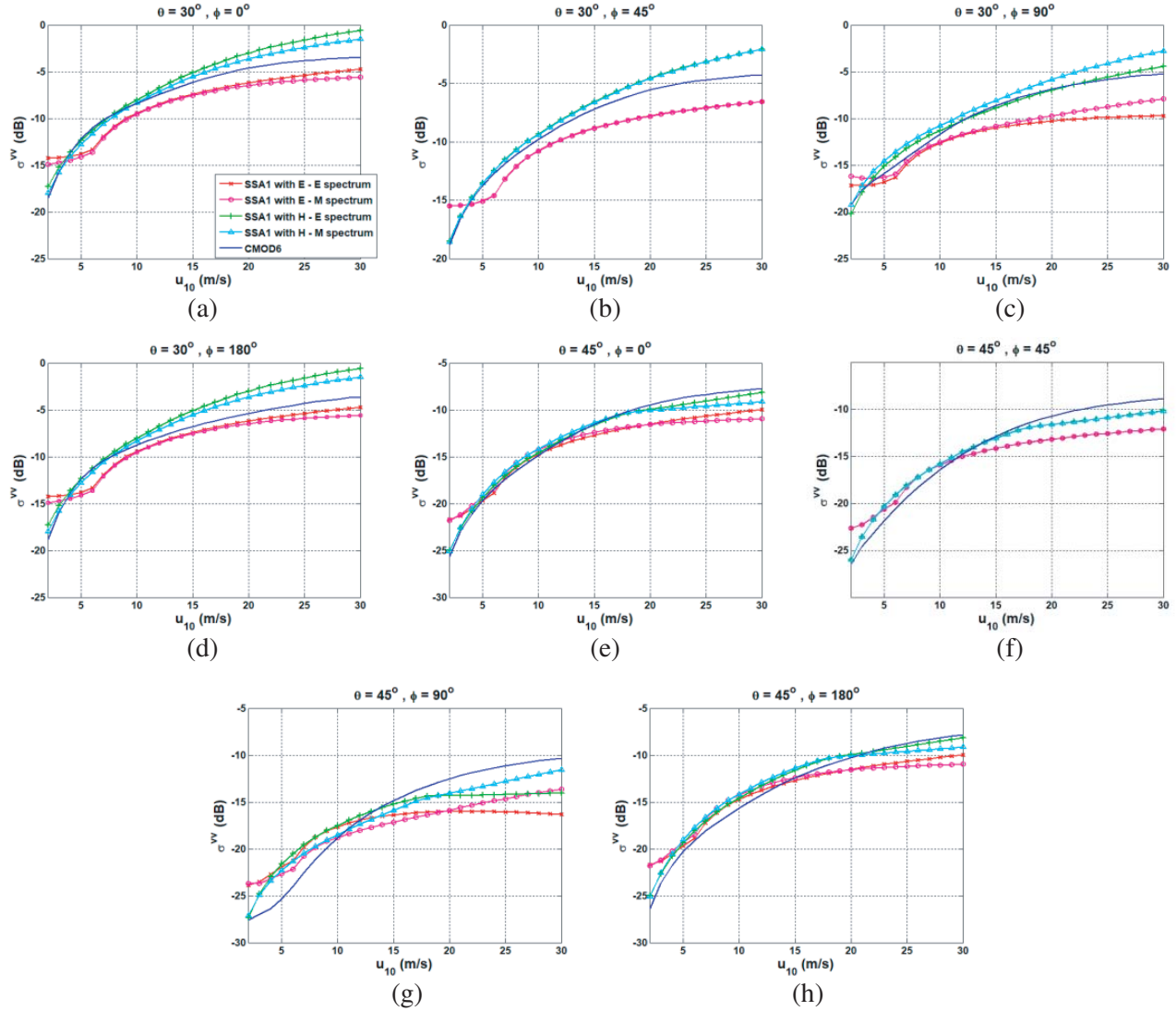


Figure 3. Backscattering NRCS in terms of wind speed; for incident angle 30° and wind directions $\varphi =$ (a) 0° , (b) 45° , (c) 90° and (d) 180° for incident angle 45° and wind directions $\varphi =$ (e) 0° , (f) 45° , (g) 90° and (h) 180° .

and (g), the curves of Elfouhaily omnidirectional spectrum do not have good behaviour in crosswind direction. In general, the Hwang curves have more agreements with CMOD6 curves, but in downwind direction, the Elfouhaily curves have better performance about the incident angle of 30° , and by increasing the incident angle the accuracy of Hwang curves is improved. According to the curves, though at low wind speeds, a small difference between NRCS values leads to the small error in wind speed determination, the same difference at high wind speeds can lead to a large error in wind speed determination. Therefore, at very high wind speeds (> 20 m/s), the SSA1 model with none of the spectra is not trustworthy for most situations.

In detail, in the upwind direction ($\varphi = 0^\circ$, the H-E curve is close to CMOD6 curve at low wind speeds. At moderate and high wind speeds, the H-M curve is close to CMOD6 curve at the incident angle of 30° , and by increasing the incident angle to 45° the H-E curve gets close to CMOD6 curve. In crosswind direction ($\varphi = 90^\circ$, the H-E curve is close to CMOD6 curve at the incident angle of 30° , and by increasing the incident angle, the H-M curve gets close to CMOD6 curve, at all wind speed range. In downwind direction ($\varphi = 180^\circ$, for the incident angle of 30° the H-E and H-M curves are close to

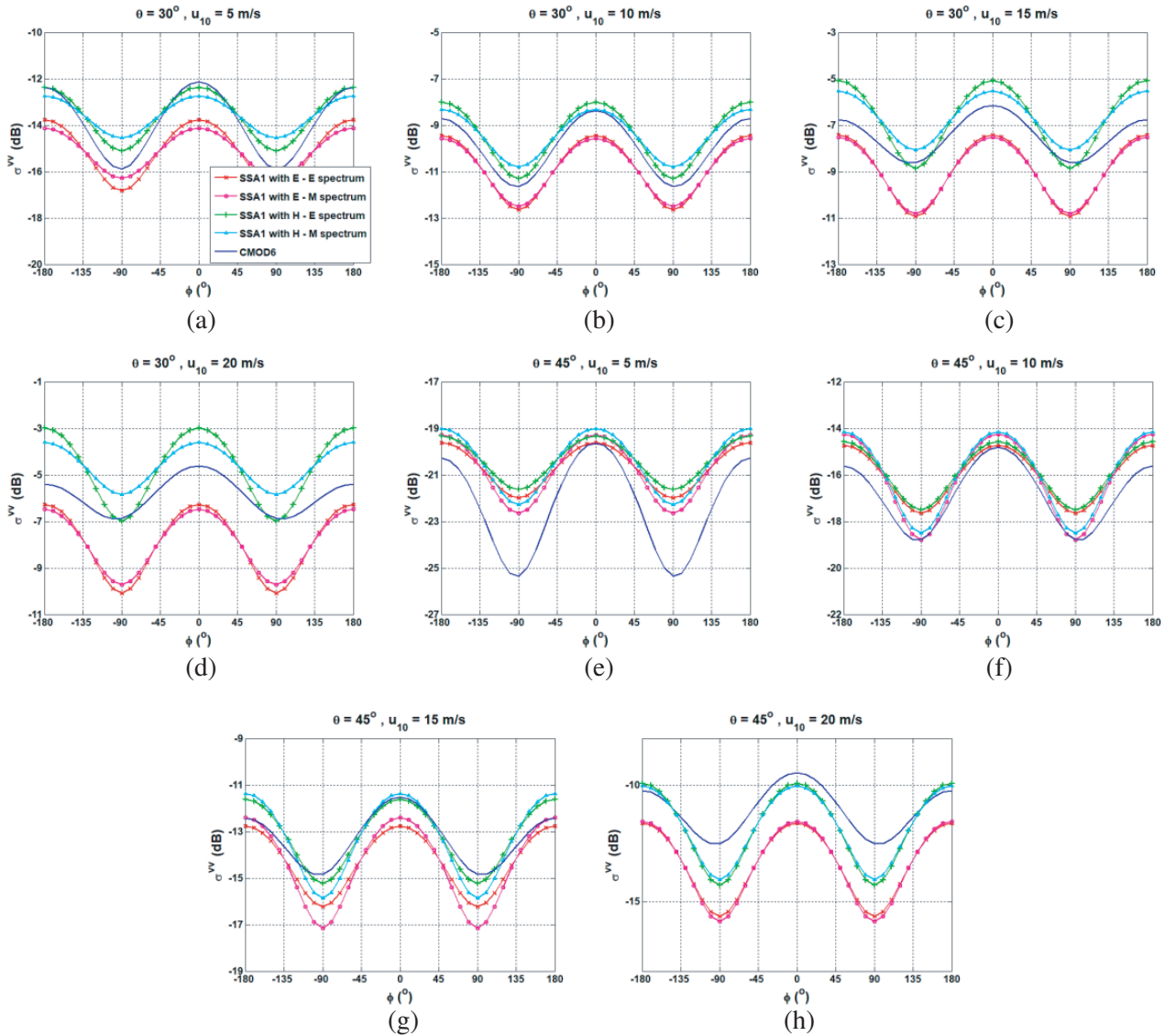


Figure 4. Backscattering NRCS in terms of wind direction; for incident angle 30° and wind speeds $u_{10} =$ (a) 5 m/s, (b) 10 m/s, (c) 15 m/s and (d) 20 m/s, for incident angle 45° and wind speeds $u_{10} =$ (e) 5 m/s, (f) 10 m/s, (g) 15 m/s and (h) 20 m/s.

CMOD6 curve at low wind speeds, and E-E curve is close to CMOD6 curve at moderate and high wind speeds. By increasing the incident angle, the H-E curve gets close to CMOD6 curve at most of wind speed ranges.

The VV -polarized backscattering NRCSs in terms of wind direction are plotted in Fig. 4 for wind speeds of 5, 10, 15, and 20 m/s and at incident angles of 30° and 45° . Fig. 4 shows that all the curves have similar behaviours with respect to wind direction variations. None of the curves match CMOD6 curve. However, the Hwang spectrum has a better condition than Elfouhaily spectrum in most situations. About the Elfouhaily and McDaniel spreading functions, it cannot be said that one of them is more accurate than another. Though it seems that the fluctuations related to McDaniel function are more similar to CMOD6 than Elfouhaily function, in composition with the omnidirectional spectra, in some situations, the Elfouhaily function has better performance than the McDaniel function, and in some other situations, the McDaniel function has better performance than the other one. According to Figs. 3 and 4, the best choice for spectrum in various situations at C-band and vertical polarization is

Table 1. Most accurate spectra for various wind speed and direction ranges and variation of incident angle from $30^\circ \rightarrow 45^\circ$.

Wind speed (m/s)	Wind direction ($^\circ$)			Sea spectrum for $\theta = 30^\circ \rightarrow \theta = 45^\circ$
	0–45	45–135	135–180	
< 5	H-E	H-E \rightarrow H-M	H-E	
5–10	H-E	E-M	H-M \rightarrow H-E	
10–15	H-M \rightarrow H-E	H-E \rightarrow H-M	E-E	
15–20	H-M \rightarrow H-E	H-E	E-E \rightarrow H-E	

given in Table 1.

The real sea surface profile is a non-Gaussian stochastic process, and the backscattered signal for upwind direction is larger than that for downwind direction. Whereas the amount of difference is low, and its effect on the accuracy of retrieved wind speed is low, in the scattering model of this work, the Gaussian statistics is assumed for surface roughness, which leads to up/downwind symmetry. This simplification is acceptable at low and moderate wind speeds. By applying the nonlinear surfaces such as choppy wave model [19] or Creamer model [20] and the resulting non-Gaussian statistics, the accuracy of the scattering model increases. The breaking waves are the marine phenomena that can have effect on scattering from the sea surface. In [16] it is shown that in C-band frequency, the breaking waves have no effect on *VV*-polarized backscattering. Accordingly, the breaking wave effects on sea surface scattering is not considered in this work.

4. WIND SPEED RETRIEVAL

For a better understanding of the error amount in wind estimation by the analytical model with various spectra, we retrieve the wind speed from SAR images. We employ the scatterometry-based approach for wind speed retrieval. In this approach, by minimizing the difference between the NRCS of SAR image and the NRCS of theoretical or empirical models for a given wind direction, the wind speed is retrieved. The required wind directions for this approach are provided by either the SAR image itself or outside resources, e.g., weather prediction model.

4.1. Sentinel-1A SAR Data

Three *VV*-polarized NRCS images from a part of Persian Gulf acquired on February 01, 2018 from 2:38:56 to 2:39:21 UTC, February 13, 2018 from 2:38:56 to 2:39:21 UTC, and December 22, 2018 from 2:39:04 to 2:39:29 UTC are used for wind retrieval (Figs. 5(a), (b) and (c)). The radar footprint on the Persian Gulf can be seen in Fig. 5(d). The Geo-coordinates of corners of images are ($29^\circ 4' 51''\text{N}$, $51^\circ 4' 13''\text{E}$), ($29^\circ 9' 36''\text{N}$, $48^\circ 8' 20''\text{E}$), ($27^\circ 4' 24''\text{N}$, $50^\circ 4' 36''\text{E}$), and ($28^\circ 9' 19''\text{N}$, $48^\circ 0' 40''\text{E}$). The images are acquired by *IWS* mode with the incident angle range of $30\text{--}45^\circ$. The level-1 data are selected, and the images are acquired with the ground range detected (GRD) mechanism. The dimensions of original images are approximately $256\text{ km} \times 167\text{ km}$ corresponding to 25664×16728 pixels. The pixel sizes are 10 m and 10 m in azimuth and range directions, respectively.

4.2. Weather Data

The Icosahedral Nonhydrostatic (ICON) model is a global numerical weather prediction (NWP) model produced by Germany weather service (DWD). We use the wind direction information given by this model on February 01, February 13, and December 22, 2018 at 3:00 UTC with the spatial resolution of 13 km as shown in Fig. 6. The time difference between weather model and SAR imagery is about 20 min.

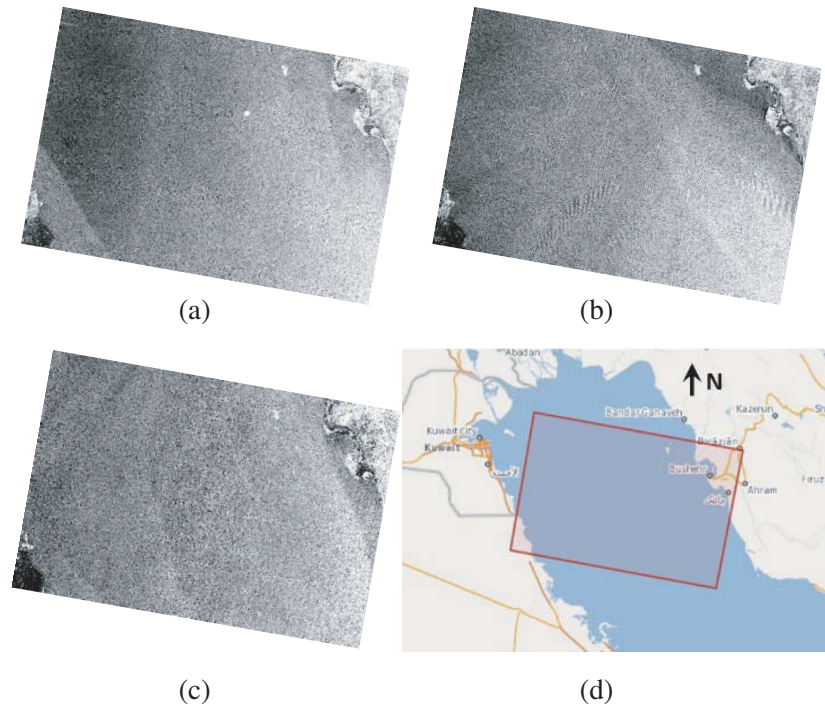


Figure 5. VV-polarized NRCS images (a) on 2018/02/01 from 2:38:56 to 2:39:21 UTC, (b) on 2018/02/13 from 2:38:56 to 2:39:21 UTC, (c) on 2018/12/22 from 2:38:56 to 2:39:21 UTC, (d) the radar footprint on Persian Gulf is shown by rectangular [29].

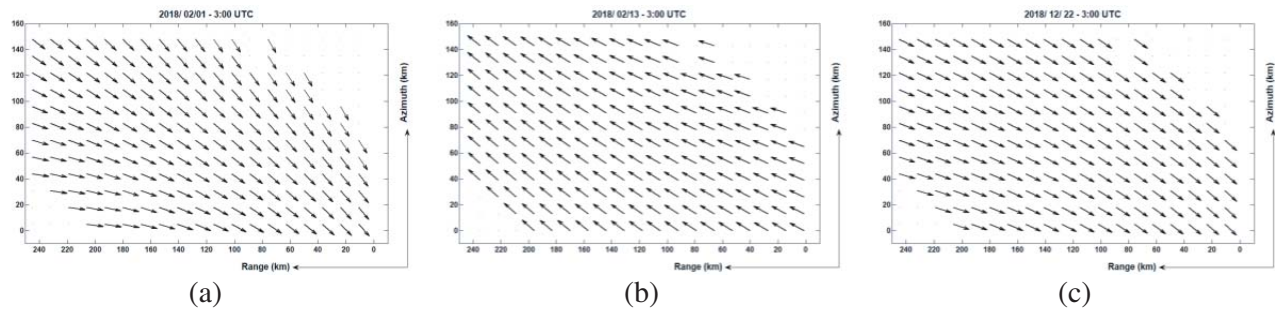


Figure 6. Wind directions given by ICON model in 13 km resolution in the region of SAR imagery on (a) 2018/02/01, (b) 2018/02/13, (c) 2018/12/22 at 3:00 UTC.

4.3. Wind Speed Retrieval

According to the spatial resolution of the weather model, the dimensions of wind vector cells (WVC) are chosen as 13 km × 13 km. Before inversion, using the Sentinels Application Platform (SNAP) software, the images are calibrated; the speckle noise is removed; and the mean NRCS is obtained for each WVC, by the multi-looking method. The land zones and the pixels with no data are removed. According to the valid region for inversion, the number of WVCs in each image is 202.

The CMOD6 is considered as a reference model, and the retrieved wind speeds by the SSA1 model with different spectra versus the retrieved wind speeds by CMOD6 are plotted in Fig. 7. The values of error metrics are given in the figure, including root mean square error (RMSE), mean bias (Bias), and correlation (R). The results show good agreement between the SSA1 model with various spectra and CMOD6. The values of RMSE and Bias are smaller than 1.5 m/s and ~ 1 m/s, respectively, and the results of the two methods are highly correlated ($R \geq 0.89$). At low wind speeds (< 5 m/s), the

Elfouhaily spectrum, unlike the Hwang spectrum, have no agreement with CMOD6. At moderate and high wind speeds, the accuracy of different spectra depends on wind direction and radar incidence angle. For more details, in Fig. 8, the estimated wind speeds at the incident angles about 30° and 45° are separated according to wind direction ranges.

Figures 8(a), (b), and (c) correspond to the incident angles about 30°, and Figs. 8(d) and (e)

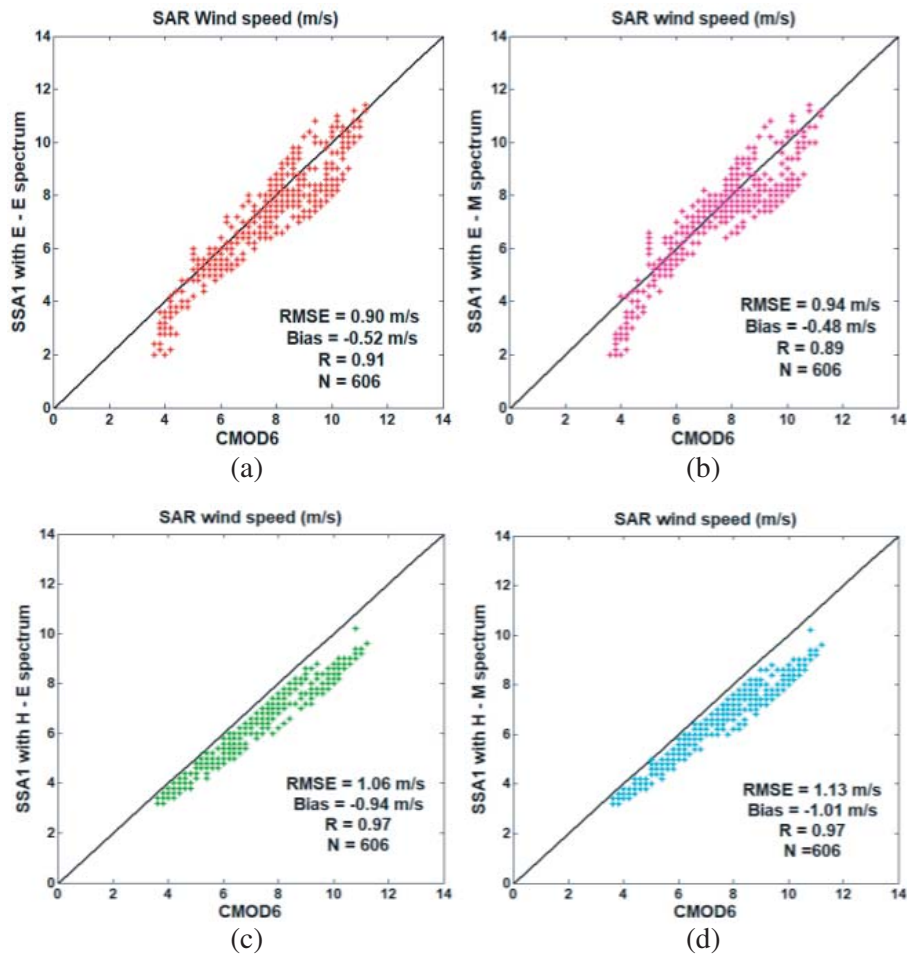
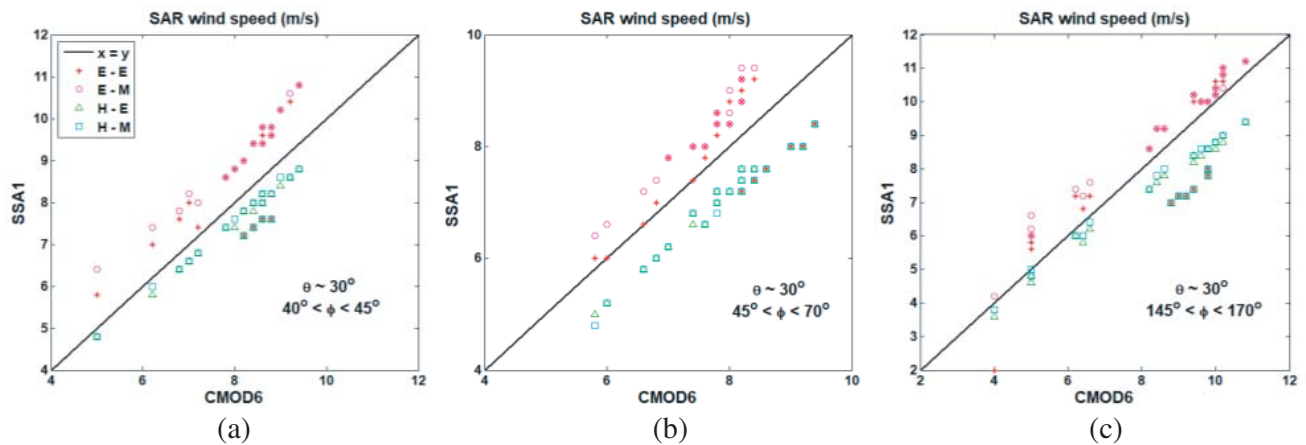


Figure 7. Wind speed retrieved by the SSA1 model with various spectrums versus wind speed retrieved by CMOD6.



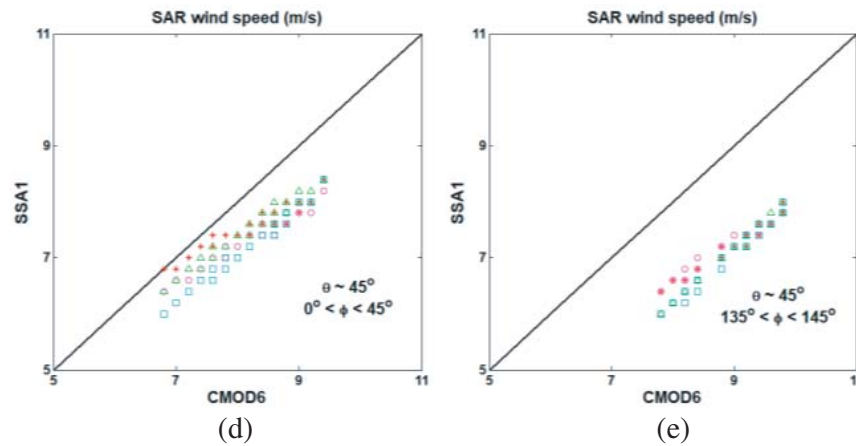


Figure 8. SAR wind speeds retrieved by SSA1 with various spectra versus CMOD6 wind speed (a) $\theta = 30^\circ$, $40^\circ < \varphi < 45^\circ$, (b) $\theta = 30^\circ$, $45^\circ < \varphi < 70^\circ$, (c) $\theta = 30^\circ$, $145^\circ < \varphi < 170^\circ$, (d) $\theta = 45^\circ$, $0^\circ < \varphi < 45^\circ$, (e) $\theta = 135^\circ$, $0^\circ < \varphi < 145^\circ$.

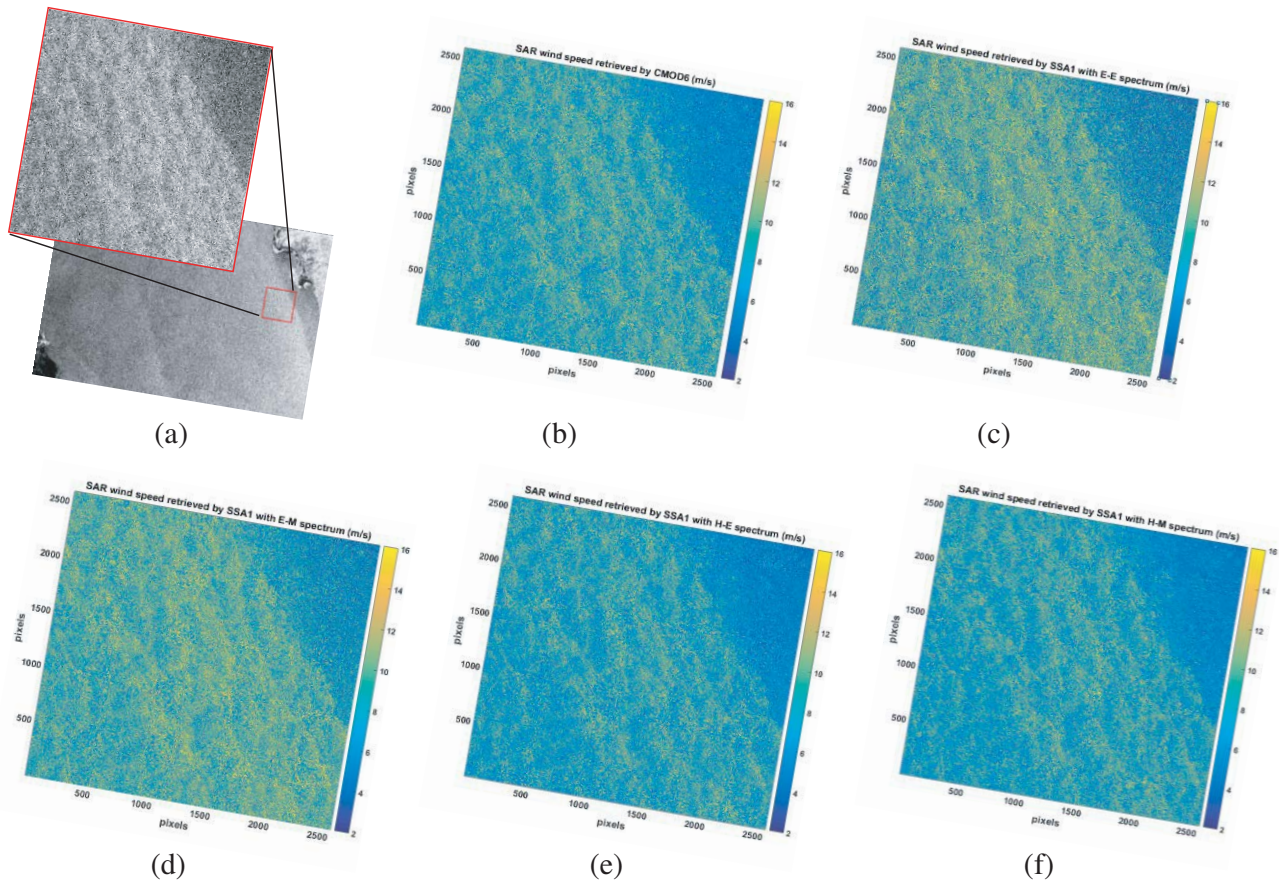


Figure 9. (a) ROI of NRCS image on 2018/12/22, Wind speeds retrieved from SAR image in $10\text{ m} \times 10\text{ m}$ pixels by (b) CMOD6, (c) the SSA1 model and E-E spectrum, (d) the SSA1 model and E-M spectrum, (e) the SSA1 model and H-E spectrum and (f) the SSA1 model and H-M spectrum. Color bar indicates u_{10} (2–16 m/s).

correspond to the incident angles about 45° . In this evaluation, the wind speed range is lower than 12 m/s. In Fig. 8(a), in which wind direction is smaller than 45° , the H-M spectrum is more accurate than other spectra. Fig. 8(b) shows that E-E spectrum has the best performance at the wind directions between 45° and 70° . Fig. 8(c) shows better performances of the H-E and H-M spectra for lower wind speeds and better performances of the E-E and E-M spectra for higher wind speeds at the wind directions between 145° and 170° . In Fig. 8(d), in which the wind directions are smaller than 45° , the E-E shows better performance for lower wind speeds, and by increasing the wind speed, four spectra show similar performances. It is seen in Fig. 8(e) that the E-M spectrum is relatively more accurate than others at the wind directions between 135° and 145° .

Then, a part of the original image acquired on December 22, 2018, from a region of interest (ROI) is considered for high-resolution wind speed retrieval. The dimensions of ROI are $26 \text{ km} \times 26 \text{ km}$ (equivalent to four WVCs), shown in Fig. 9(a). The pixels size of the original image is $10 \text{ m} \times 10 \text{ m}$; therefore, the ROI includes 2600×2600 pixels. It is assumed that the wind direction in the pixels of each WVC is constant and equal to the wind direction of that WVC. Then, the wind speeds are estimated by inverting the CMOD6 and the SSA1 model with various spectra as seen in Figs. 9(b) to (f). The wind direction in ROI is about 40° , and the incident angle is about 30° . According to the figure, the results of the H-E and H-M spectra (Figs. 9(e) and (f)) are similar to CMOD6 results (Fig. 9(b)), and the E-E and E-M spectra (Figs. 9(c) and (d)) overestimate the wind speeds at high winds. Whereas the wind direction is about 45° , the effect of the angular spreading function is low.

5. CONCLUSION

In this paper, the analytical scattering model of SSA1 is employed for the sea surface wind speed estimating from Sentinel-1A VV-polarized SAR images. The accuracy of sea spectrum has undeniable effects on the accuracy of the analytical scattering coefficients. Among the various spectra proposed in the literature, we choose Elfouhaily spectrum as the most common directional spectrum and Hwang spectrum as the newest omnidirectional spectrum to evaluate their accuracy for our sea scattering problem. In addition to Elfouhaily spreading function, we use the McDaniel spreading function to see the effect of directionality in the accuracy of the results. The comparisons of the Elfouhaily omnidirectional spectrum with the Hwang spectrum show more power of Hwang spectrum at high winds, and comparisons of the Elfouhaily spreading function with the McDaniel function show greater directionality of McDaniel function at high wavenumbers. Then, the SSA1 simulations are performed with the E-E, E-M, H-E, and H-M composite spectra. The comparison of the backscattering NRCSs of sea surface simulated by the SSA1 model using four spectra with the empirical function CMOD6 shows that the various spectra have different performances in different situations depending on wind speed, wind direction, and incident angle. From the viewpoint of the omnidirectional spectrum, Hwang spectrum has better performance in most cases. From the viewpoint of angular function, in some conditions, the Elfouhaily function has better performance than the McDaniel function, and in some other conditions, better performance belongs to the McDaniel function. Among the composite spectra, the H-E spectrum is more accurate than others in more situations. At very high wind speeds ($> 20 \text{ m/s}$), differences between the SSA1 model with various spectra and CMOD6 are high in most situations and lead to a large error in wind speed estimation.

Then, the wind speeds are retrieved from SAR data by employing the scatterometry-based approach. By using the wind directions information extracted from ICON weather prediction model, the SSA1 models with four various spectra are inverted, and the results are compared with the wind speeds retrieved by inverting the CMOD6. In the first case, the spatial resolution of the images is reduced to 13 km according to the resolution of the ICON model. The results and error values show the good accuracy of the analytical model in the estimation of the wind speeds. Detailed comparisons show different performances of the spectra at different incident angles and different wind speeds and direction ranges corresponding to utilized SAR images. At the second case, the wind speeds are retrieved from a part of original high-resolution SAR images. For the case, the wind speeds retrieved by the SSA1 with Hwang spectrum have good agreement with the CMOD6 results, and Elfouhaily spectrum overestimates the wind speeds at high winds.

As results, the analytical model SSA1 can be used for estimating the wind speeds below 20 m/s from

VV-polarized Sentinel-1A SAR data as well as CMOD6 function. According to the better performance of the Hwang spectrum in most situations, this spectrum is suggested to use for wind speed retrieval. By employing the second-order accuracy of SSA and nonlinear surfaces and by considering some marine phenomena such as the foam effects at high wind speeds, the accuracy of wind speed retrieval is increased. Also, other theoretical methods such as the TSM can be tested for wind speed retrieval in high accuracy.

REFERENCES

1. Hersbach, H., "CMOD5 an improved geophysical model function for ERS C-band scatterometry," *ECMWF Technical Memorandum*, 395, Technical report, ECMWF, Jan. 2003.
2. Hersbach, H., "CMOD5.N a C-band geophysical model function for equivalent neutral wind," *ECMWF Technical Memorandum*, 554, Technical report, ECMWF, Apr. 2008.
3. Elyouncha, A., X. Neyt, A. Stoffelen, and J. Verspeek, "Assessment of the corrected CMOD6 GMF using scatterometer data," *Proc. SPIE*, Vol. 9638, No. 3, 11 pages, Oct. 2015.
4. Monaldo, F., C. Jackson, X. Li, and W. G. Pichel, "Preliminary evaluation of Sentinel-1A wind speed retrievals," *IEEE J. Sel. Topics Appl. Earth Observ. Remote Sens.*, Vol. 9, No. 6, 2638–2642, 2016.
5. La, T. V., A. Khenchaf, F. Comblet, and C. Nahum, "Exploitation of C-band Sentinel-1 images for high-resolution wind field retrieval in coastal zones (Iroise coast, France)," *IEEE J. Sel. Topics Appl. Earth Observ. Remote Sens.*, Vol. 10, No. 12, 5458–5471, Dec. 2017.
6. Mouche, A. and B. Chapron, "Global C-band Envisat, RADARSAT-2 and Sentinel-1 SAR measurements in copolarization and cross-polarization," *J. Geophys. Res. Oceans*, Vol. 120, 7195–7207, doi: 10.1002/2015JC011149, 2015.
7. Lu, Y., B. Zhang, W. Perrie, A. A. Mouche, X. Li, and H. Wang, "A C-band geophysical model function for determining coastal wind speed using synthetic aperture radar," *IEEE J. Sel. Topics Appl. Earth Observ. Remote Sens.*, Vol. 11, No. 7, 2417–2428, 2018.
8. Miret, D., G. Soriano, and M. Saillard, "Rigorous simulations of microwave scattering from finite conductivity two-dimensional sea surfaces at low grazing angles," *IEEE Trans. Geosci. Remote Sens.*, Vol. 52, No. 6, 3150–3158, Jun. 2014.
9. Hastings, F. D., J. B. Schneider, and S. L. Broschat, "A Monte-Carlo FDTD technique for rough surface scattering," *IEEE Trans. Antennas Propag.*, Vol. 43, No. 11, 1183–1191, Nov. 1995.
10. Tsang, L., J. A. Kong, and K. H. Ding, *Scattering of Electromagnetic Waves, Vol. 1: Theory and Applications*, Wiley, Hoboken, NJ, USA, 2000.
11. Tsang, L. and J. A. Kong, *Scattering of Electromagnetic Waves, Vol. 3: Advanced Topics*, Wiley, Hoboken, NJ, USA, 2001.
12. Yang, X., Y. Du, Z. Li, and K. S. Chen, "Investigation of bistatic radar scattering from sea surfaces with breaking waves," *2017 IEEE International Geoscience and Remote Sensing Symposium (IGARSS)*, 2017.
13. Soriano, G. and C. A. Guérin, "A cutoff invariant two-scale model in electromagnetic scattering from sea surfaces," *IEEE Geosci. Remote Sens. Lett.*, Vol. 5, No. 2, 199–203, Apr. 2008.
14. McDaniel, S. T., "Small-slope predictions of microwave backscatter from the sea surface," *Waves in Random Media*, Vol. 11, No. 3, 343–360, doi: 10.1080/13616670109409789, 2001.
15. Voronovich, A. G., "Small-slope approximation for electromagnetic wave scattering at a rough interface of two dielectric half-spaces," *Waves in Random Media*, Vol. 4, No. 3, 337–367, Jul. 1994.
16. Voronovich, A. G. and V. U. Zavorotny, "Theoretical model for scattering of radar signals in Ku- and C-bands from a rough sea surface with breaking waves," *Waves in Random Media*, Vol. 11, No. 3, 247–269, 2001.
17. Bourlier, C. and N. Pinel, "Numerical implementation of local unified models for backscattering from random rough sea surfaces," *Waves in Random and Complex Media*, Vol. 19, No. 3, 455–479, Aug. 2009.

18. Voronovich, A. G. and V. U. Zavorotny, "Full-polarization modeling of monostatic and bistatic radar scattering from a rough sea surface," *IEEE Trans. Antennas Propag.*, Vol. 62, No. 3, 1362–1371, Mar. 2014.
19. Nouguier, F., C. A. Guérin, and B. Chapron, "Scattering from nonlinear gravity waves: The "Choppy wave" model," *IEEE Trans. Geosci. Remote Sens.*, Vol. 48, No. 12, 4184–4192, Dec. 2010.
20. Li, X. and X. Xu, "Scattering and Doppler spectral analysis for two-dimensional linear and nonlinear sea surfaces," *IEEE Trans. Geosci. Remote Sens.*, Vol. 49, No. 2, 603–611, Feb. 2011.
21. Apel, J. R., "An improved model of the ocean surface wave vector spectrum and its effects on radar backscatter," *J. Geophys. Res. Oceans*, Vol. 99, 16269–16291, 1994.
22. Romeiser, R., W. Alpers, and V. Wismann, "An improved composite surface model for the radar backscattering cross section of the ocean surface: 1. Theory of the model and optimization/validation by scatterometer data," *J. Geophys. Res. Oceans*, Vol. 102, 25237–25250, 1997.
23. Elfouhaily, T., B. Chapron, K. Katsaros, and D. Vandemark, "A unified directional spectrum for long and short wind-driven waves," *Journal of Geophysical Research*, Vol. 102, No. C7, 15,781–15,796, Jul. 15, 1997.
24. Hwang, P. A., "Observations of swell influence on ocean surface roughness," *J. Geophys. Res. Oceans*, Vol. 113, C12024, 2008.
25. Hwang, P. A., "A note on the ocean surface roughness spectrum," *J. Atmos. Ocean. Technol.*, Vol. 28, 436–443, 2011.
26. Hwang, P. A., D. M. Burrage, D. W. Wang, and J. C. Wesson, "Ocean surface roughness spectrum in high wind condition for microwave backscatter and emission computations," *J. Atmos. Ocean. Technol.*, Vol. 30, 2168–2188, 2013.
27. Hwang, P. A. and F. Fois, "Surface roughness and breaking wave properties retrieved from polarimetric microwave radar backscattering," *J. Geophys. Res. Oceans*, Vol. 120, 3640–3657, 2015.
28. Ellison, W., A. Balana, G. Delbos, K. Lamkaouchi, L. Eymard, C. Guillou, and C. Prigent, "New permittivity measurements of seawater," *Radio Sci.*, Vol. 33, 639–648, 1998.
29. [Online]. Available: <https://scihub.copernicus.eu/dhus/#/home>.